Comprehensive study of the interstitial hydrogen donor in SnO$_2$

F. Herklotz[*] and E. V. Lavrov

TU Dresden University of Technology, Institute of Applied Physics, 01062 Dresden, Germany

V. V. Melnikov

Department of Metal Physics, Tomsk State University, 634050 Tomsk, Russia

Z. Galazka

Leibniz Institute for Crystal Growth, Max-Born-Str. 2, 12489 Berlin, Germany

V. F. Agekyan

Department of Solid State Physics, St. Petersburg State University, 108504 St. Petersburg, Russia

The nature of interstitial hydrogen in SnO$_2$ has been inferred by a combined study of first-principles theory and infrared absorption, near band edge absorption, and photoluminescence spectroscopy. The earlier interpretation of a center with an O–H stretch mode at 3156 cm^{-1} as interstitial hydrogen is confirmed. Uniaxial stress experiments on the 3156 cm^{-1} mode reveal that the interstitial hydrogen atom is located in the open c channel of the rutile SnO$_2$ structure. Migration along the c axis of the crystals occurs via low barrier hydrogen jumps of around 0.57 eV to symmetrically equivalent nearest-neighbor positions. Combinational vibrations of the O–H stretch mode with the out-of-ab-plane and in-ab-plane wag modes at about 4014 and 4332 cm^{-1} have been identified. Free carrier absorption and excitonic properties of the defect demonstrate that H$_i$ forms an effective shallow-donor-like state similar to the well-characterized F, Cl, and Sb n-type dopants in this material.

I. INTRODUCTION

SnO$_2$ stands out as a wide bandgap material with immense promise for a wide range of electronic and optoelectronic device applications, such as transparent conductor electronics [1,2], solar cells [3], gas sensors [4,5], catalysis [4], and even spintronics [6]. However, the full realization of its potential has been hindered by the persistent challenge of controlling its electrical conductivity. Typically, SnO$_2$ exhibits unipolar n-type behavior. Identifying and characterizing the underlying cause of this intrinsic n-type conductivity are of paramount importance for enhancing the performance of existing SnO$_2$-based devices and enable new ones.

Historically, the n-type bevavior of SnO$_2$ has often been attributed to intrinsic point defects such as O vacancies and Sn interstitials [7–11]. Recent theoretical findings challenge the notion that native defects are solely responsible for this conductivity [12,13]. Instead, it has become increasingly evident that hydrogen, being not only the most abundant but also an unavoidable impurity, frequently plays a pivotal role in governing both the electrical and optical characteristics of the material [12–17].

First-principles calculations have revealed that interstitial hydrogen (H$_i$) exhibits a low formation energy and behaves as a shallow donor in SnO$_2$ [12,15–17]. It forms a strong dative bond with oxygen, characterized by an O–H bond oriented perpendicular to the [001] axis within the open c channels of the rutile SnO$_2$ structure. The calculated migration barrier of H$_i$ is remarkably low, at just 0.57 eV, implying that interstitial hydrogen exhibits high mobility at room temperature. Supporting these conclusions, shallow donor states of hydrogen have been reported in conductivity and transport measurements after intentional introduction of hydrogen into SnO$_2$ [18,19], as well as from muon spin-rotation spectra [20].

Early IR absorption experiments on SnO$_2$ unveiled a variety of hydrogen-related defects, identifiable by their local vibrational signature [17,21–26]. Of particular relevance to this investigation is a defect responsible for a local vibrational mode (LVM) at 3156 cm^{-1} (measured at 10 K), originating from an O–H bond oriented perpendicular to the c axis of the crystal. This defect has commonly been attributed to H$_i$, as polarization and thermal stability data align with the aforementioned theoretical predictions on this defect [17,21,27]. However, experiments capable of independently verifying the microscopic structure of the 3156 cm^{-1} defect and elucidating its diffusion properties are currently lacking.

The primary objective of this study is to elucidate the structure, motion and electrical activity of interstitial hydrogen in SnO$_2$. To achieve this, we have conducted a comprehensive spectroscopic investigation, encompassing vibrational mode spectroscopy, stress-induced dichroism, band-edge absorption, and photoluminescence studies, all focused on the H$_i$

*frank.herklotz1@tu-dresden.de

donor in SnO$_2$ and complemented by first-principles calculations. The results confirm that interstitial hydrogen in SnO$_2$ corresponds to the 3156 cm^{-1} center and forms an effective shallow-donor-like state in this material.

II. METHODS

A. Sample preparation

The SnO$_2$ samples utilized in this study were nominally undoped *n*-type single crystals, grown through two different methods: chemical vapor transport (CVT) [28,29] and physical vapor transport (PVT) [30–32].

The CVT-grown samples were produced using the chemical reaction SnCl$_4$ + H$_2$ = SnO$_2$ + HCl at 1200 °C. Argon gas served as a transport agent for the SnCl$_4$ and H$_2$ vapors. These crystals typically exhibited *n*-type behavior with high conductivity. To reduce the free electron concentration, post-growth heat treatments were applied, involving temperatures above 900 °C in an air environment. The CVT-grown samples were characterized by high purity and good structural quality [28].

The PVT-grown samples used in this study were initially *n*-type semiconductors without any intentional doping. Hall effect measurements revealed a free electron concentration of approximately 10^{18} cm^{-3} and an electron mobility ranging from 125 to 160 cm^2 V^{-1} s^{-1} [32]. To convert these semiconducting samples into electrically insulating ones, they underwent heat treatments at temperatures between 1000 and 1100 °C for durations of 12 to 20 hours in an air atmosphere. PVT-grown samples exhibited good structural quality and high purity due to the direct vapor transport of SnO, which reacts with oxygen to form SnO$_2$ crystals [30,31].

The SnO$_2$ crystals had dimensions of approximately 4 × 4 mm^2 with a thickness ranging from 0.4 to 0.8 mm. To introduce hydrogen into the samples, we employed thermal treatments at temperatures ranging from 600 °C to 700 °C for 1 hour in a sealed quartz ampule. The ampule was concurrently loaded with a drop of H$_2$O and H$_2$ gas (pressure of 0.01 to 0.1 bar at room temperature). Unlike treatments in pure H$_2$ gas [17,21], this procedure resulted in "hydrogenated" samples with no discernible surface damage. Isochronal thermal treatments ("annealings") were conducted in the temperature range of 100 °C to 860 °C in an argon ambient for 30 minutes, followed by a rapid cool-down to room temperature in approximately 2 minutes.

B. IR absorption

Infrared (IR) absorption spectra were acquired using a Bomem DA3.01 Fourier transform spectrometer equipped with a globar light source, a CaF$_2$ beam splitter, and a liquid-nitrogen-cooled InSb detector. The spectral resolution was set at 0.5 to 1 cm^{-1}. Unless stated otherwise, the sample temperature was stabilized within the range of 14 to 18 K in a He gas-flow cryostat equipped with KBr windows. Polarized light was supplied using a wire-grid polarizer with a KRS-5 substrate. For IR absorption measurements under uniaxial stress, the samples were cut to dimensions of approximately 3 × 1.5 × 0.5 mm^3, with the sample axes aligned parallel to the [100], [010], and [001] crystallographic directions,

respectively. A custom-designed stress rig mounted within the cryostat enabled the application of stress along the [100] axis of the sample.

C. Excitonic absorption

Spectrophotometric measurements of absorption with ultraviolet (UV) light in the spectral region corresponding to the fundamental excitonic transitions of SnO$_2$ (approximately 3.6 eV) were performed. This was achieved using a 150 W Xenon short-arc (XBO) light source, a 1 m single grating monochromator equipped with a 1200 lines/mm grating, and a Peltier-cooled photomultiplier. The spectral resolution was approximately 0.5 meV at 3.6 eV. The sample temperature was stabilized within 0.2 K in the range of 9 to 60 K using a He gas-flow cryostat fitted with sapphire windows. To establish a reference spectrum, a nominally undoped "hydrogen-free" SnO$_2$ sample was employed.

D. Photoluminescence

For photoluminescence (PL) measurements, the samples were mounted in a liquid He cryostat and excited using the 325 nm line of a HeCd laser with a typical excitation power of 10 mW. The emitted light was dispersed by a 1 m single grating monochromator equipped with a 1200 lines/mm grating and detected with a Peltier-cooled photomultiplier. The spectral resolution was approximately 0.5 meV at 3.6 eV. Calibration of the monochromator was performed using the lines of a Hg lamp. Spectra were recorded within a temperature range of 4.1 to 60 K.

E. Computational details

To estimate the local structure and vibrational properties of the interstitial hydrogen defect H$_i$ in rutile SnO$_2$, we conducted first-principles calculations within the framework of density functional theory (DFT). These calculations employed the projector augmented wave (PAW) method [33] and the PBEsol exchange-correlation energy functional [34], as implemented in the QUANTUM ESPRESSO codes [35–37]. The calculated lattice constants of bulk rutile SnO$_2$, specifically a = 4.7818 Å and c = 3.2229 Å, were in reasonable agreement with the corresponding experimental values of 4.7397 and 3.1877 Å [38].

For constructing the defect model, we employed a $2a \times 2a \times 3c$ tetragonal supercell with periodic boundary conditions, comprising 24 formula units. A perspective view of the SnO$_2$ supercell along the [001] direction is shown in Fig. 1. We introduced one hydrogen atom to create the H$_i$ defect, and all atomic positions were fully relaxed.

A series of high-precision structure optimizations and subsequent calculations were conducted using a $3 \times 3 \times 3$ grid of k points. The energy cutoffs were set to 120 Ry for the plane wave basis set and 480 Ry for the fine FFT grid. Phonon modes at the Γ point were computed using density-functional perturbation theory [39]. This involved considering all possible displacements of the hydrogen atom and the oxygen atom to which it is bound.

Migration energy barriers for interstitial hydrogen diffusion were calculated using the nudged elastic band (NEB)
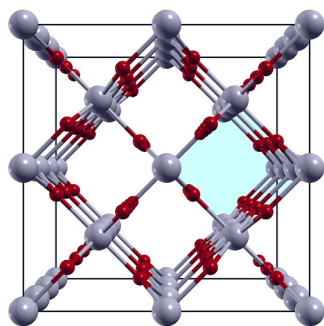
FIG. 1. Perspective view of the rutile SnO_2 supercell along the c axis: red - O, gray - Sn.

method [35,36]. Saddle points of interest were identified by exploring the full-dimensional *ab initio* potential energy surface, involving variations in all atomic positions within the supercell.

III. CALCULATIONS

The calculated local structure of the H_i defect in SnO_2 is depicted in Figs. 2 and 3. In these figures, we label the atoms as Sn_1, Sn_2, O_1, O_2, and H, all situated within a plane parallel to ab. A line connecting the Sn_1 and Sn_2 atoms closely aligns with the $\langle 100 \rangle$ direction. Consequently, an O–H bond lying in the (001) plane is oriented nearly along the [110] or [1$\bar{1}$0] directions.

The calculated equilibrium O–H bond length is approximately 1.0105 Å. The estimated vibrational frequencies of the interstitial hydrogen are 3089 cm^{-1} for the stretch mode, 1158 and 862 cm^{-1} for the in-plane and out-of-plane wag modes, respectively.

The characteristics of both the rutile SnO_2 crystal structure and its electronic properties impose limitations on the range of interstitial hydrogen motion within the crystal. The rutile structure forms channels along the [001] direction, one of which is highlighted in cyan in Fig. 1. The local structure of the H_i defect within such a tunnel is depicted in Figs. 2 and 3.

The calculated migration energy barrier between the nearest structural tunnels is approximately 2 eV, suggesting that an interstitial hydrogen is effectively trapped within the tunnel. However, the H_i defect can readily change the orientation of its O–H bond by shifting from one oxygen atom to another,
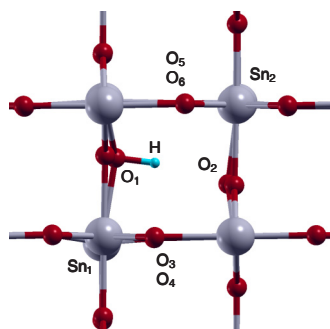

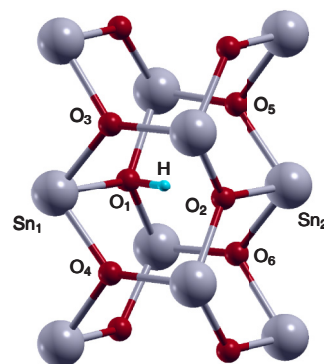FIG. 2. Local structure of the H_i defect in SnO_2: view in the ab plane.

FIG. 3. Local structure of the H_i defect in SnO_2. Atoms labeled as Sn_1, Sn_2, O_1, O_2, and H lie within the same plane parallel to ab.

as illustrated by the labeled oxygen atoms in Figs. 2 and 3. These movements can result in O–H reorientation or hydrogen diffusion along the [001] direction.

The estimated energy barrier for in-plane motion is 0.22 eV, as observed in the transition from O_1 to O_2 in Figs. 2 and 3. Transitions from O_1 to other labeled nearest oxygen atoms O_i ($i = 3, 4, 5,$ and 6) involve hydrogen motion along the c axis, with a corresponding energy barrier of approximately 0.59 eV.

Despite sharing the same energy barrier, not all transitions of the form $O_1 \rightarrow O_i$ ($i = 3, 4, 5,$ and 6) are equivalent. For instance, transitions like $O_1 \rightarrow O_3$ (equivalent to reverse transitions like $O_1 \leftarrow O_5$, etc.) exhibit varying energy gradients. Figure 4 presents interpolation of three possible path energy profiles within the structural tunnel, obtained through NEB calculations. In terms of energy gradient, transitions of the form $O_1 \rightarrow O_3$ are preferred over those of the form $O_1 \rightarrow O_5$. Therefore, under certain conditions, a spiral motion may be expected.

IV. EXPERIMENTAL RESULTS AND DISCUSSION

A. Uniaxial-stress experiments

Our calculations regarding interstitial hydrogen in SnO_2 align with two pivotal findings from prior theoretical studies [11,12,16,17]. First, it forms a hydroxyl ion, with hydrogen
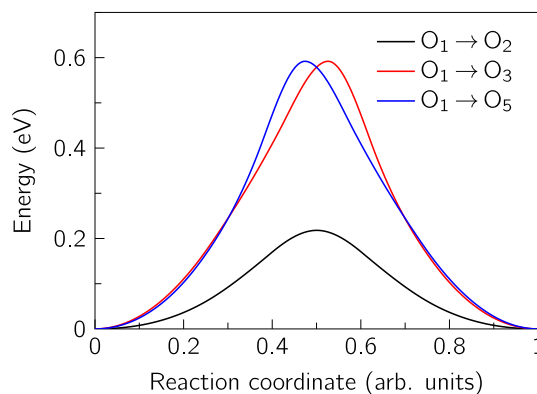

FIG. 4. Path energy profiles for three types of possible interstitial hydrogen transitions obtained in the course of the NEB calculations.
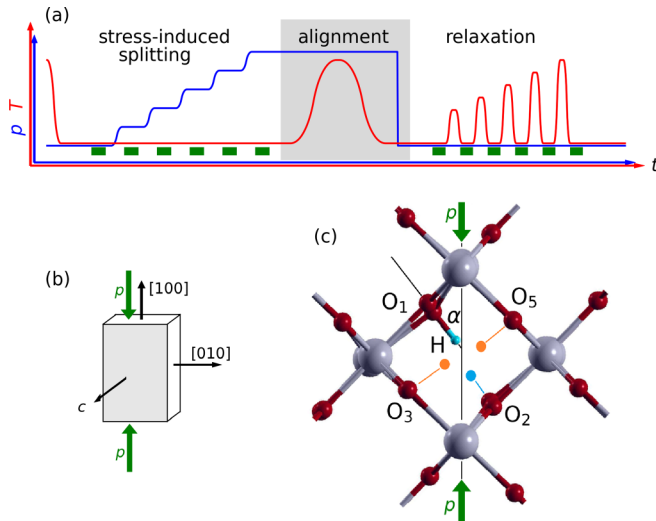
FIG. 5. Schematic representation of the stress experiments conducted. Section (a) depicts the chronological sequence of pressure p and temperature T. The green bars mark the events of measurements. Section (b) shows a sketch of the sample geometry. Section (c) presents a view in the ab plane of the local structure of H_i in SnO_2, based on the calculations presented in Sec. III. Equivalent positions of O–H bonds are marked by blue and orange colored circles. See text for more details.

FIG. 6. Sections of polarized IR absorbance spectra obtained on a hydrogenated PVT-grown SnO_2 sample during a "stress-induced splitting" experiment. The spectra are offset vertically proportional to the stress applied. See text and Fig. 5 for more details.

situated in the open c channels of the regular rutile structure of SnO_2. The O–H bond lies in the ab plane, closely aligned with the $\langle 110 \rangle$ crystallographic direction. It exhibits a relatively low stretch vibrational mode frequency compared to other hydrogen defects in this material [16,17,40]. And second, hydrogen displays high mobility even at room temperature, with migration predominantly occurring along the c channel of the SnO_2 lattice, featuring low-energy barrier jumps between neighboring O sites. The common assignment of the 3156 cm^{-1} center to H_i is based on polarization and thermal stability data being consistent with these theoretical predictions [17,21,27]. However, experiments capable of independently verifying the microscopic structure of the 3156 cm^{-1} defect and its diffusion properties are currently lacking.

Here, we address these issues using the method of stress-induced dichroism. This method has been effectively utilized to gain insights into defect properties in various materials, such as GaAs [41,42], Si [43–46], ZnO [47,48], TiO$_2$ [49,50], and In$_2$O$_3$ [51].

A schematic representation of our stress experiments is provided in Fig. 5(a), along with the sample geometry (b) and a view of the local structure of H_i (c) based on our calculations presented in Sec. III. Our experimental approach encompasses two distinct types of experiments. In the first section ("stress-induced splitting"), static stress is applied at low temperatures along the [100] axis of a c-cut SnO_2 sample. As depicted in Fig. 5(c), the original rutile lattice allows for four equivalent orientations of the O–H bond in the c channel. Applied stress lifts this orientational degeneracy, forming two pairs of nonequivalent "subgroups" labeled A (blue) and B (orange). The observed split pattern of the corresponding O–H modes under uniaxial stress serves as a crucial test for the microscopic defect model.
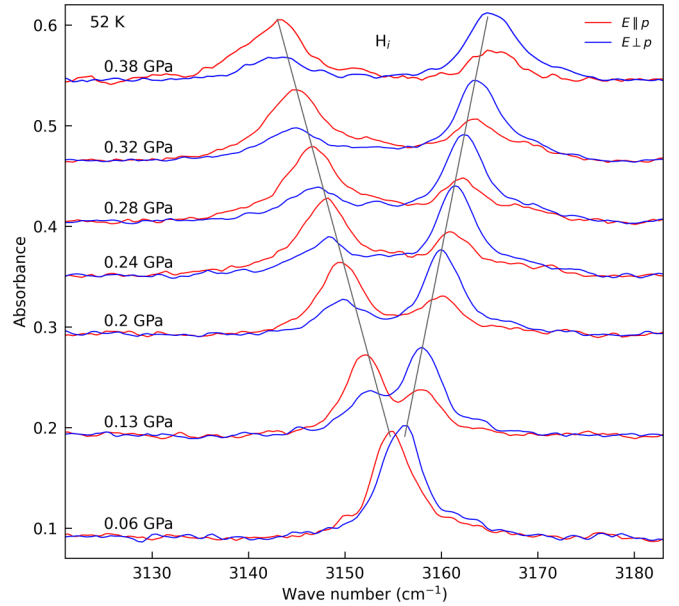
In the second part of our experiment, we achieve a nonequilibrium occupation of subgroups A and B through annealing the sample under stress ("alignment"). Subsequently, we study the thermal reorientation back to equilibrium ("relaxation") to investigate the elementary diffusion jumps of hydrogen between neighboring lattice sites.

Figure 6 displays polarized IR absorption spectra of the 3156 cm^{-1} center recorded on a hydrogenated PVT-grown SnO_2 sample during a "stress-induced splitting" experiment. The as-received PVT samples did not exhibit the 3156 cm^{-1} peak. These measurements were conducted at 52 K, where the spectra remain stable over time as the thermal energy is low enough to avoid hydrogen jumps between the A and B subgroups. The applied stress along the [100] direction results in a splitting of the mode into low-frequency and high-frequency components, predominantly polarized parallel and perpendicular to the stress direction, respectively. Both components exhibit linear shifts in frequency with the applied stress (shift rates $A_1 = -34$ cm^{-1}/GPa, $A_2 = 27$ cm^{-1}/GPa). The relative intensities of the split-off modes are approximately 2.1 : 1, inversely related for light polarized parallel and perpendicular to the stress, respectively.

The observed splitting pattern of the 3156 cm^{-1} center is consistent with the expected geometry for the H_i defect. Subgroup A comprises O–H bonds aligned at an angle α to the [100] axis. The calculated ratio for the polarized components $I_\parallel : I_\perp$ is $\cot^2 \alpha : 1$. Subgroup B, rotated by $90° - \alpha$ with respect to the [100] axis, possesses a polarization ratio of 1 : $\cot^2 \alpha$. The angle $\alpha = (34.6 \pm 0.7)°$ determined from the observed polarization ratio in our experiment closely matches the value of 37° predicted by our first-principles calculations.

Figure 7(a) shows polarized absorption spectra obtained at 52 K on the same SnO_2 sample within the "alignment" and "relaxation" experiment. The lower spectra represent
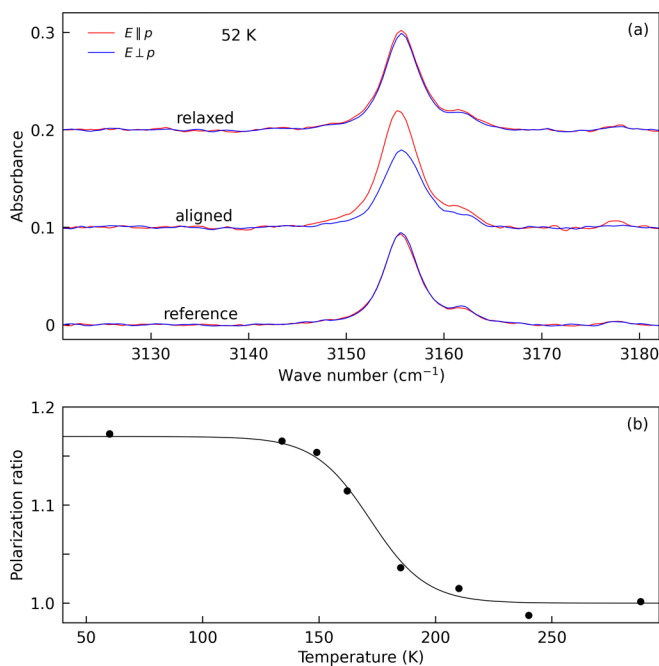
FIG. 7. (a) Polarized IR absorption spectra of a hydrogenated PVT-grown SnO$_2$ sample taken before "alignment" (reference), after "alignment" of the O–H bonds by annealing the sample under stress of 0.38 GPa at 260 K, and after "relaxation" of the O–H bonds back to thermal equilibrium by annealing the sample at 260 K with the stress released. All spectra were recorded with no stress applied. (b) The polarization ratio $I_\parallel/I_\perp$ obtained throughout a series of relaxation anneals (20 min) at progressively higher temperatures. The solid line is a guide to the eye. See text and Fig. 5 for more details.

reference measurements recorded with no applied stress before the alignment procedure. As expected, the intensity of the 3156 cm^{-1} peak for IR light polarized parallel ($I_\parallel$) and perpendicular ($I_\perp$) to the [100] axis is similar.

We found that annealing the sample under stress along [100] at temperatures above 180 K results in a distinct intensity redistribution of the polarized components. The middle spectra of Fig. 7(a) were obtained after an alignment at 260 K. It is clearly seen that the 3156-cm^{-1} defect aligns predominantly parallel to the stress. The sum of both components $I_\parallel + I_\perp$ remains constant, indicating that the applied stress does not induce reorientation of the O–H bond along the c axis or dissociation of the hydroxyl group. This alignment behavior was found consistently for annealing temperatures over approximately 170 K in both PVT and CVT-grown samples across a total of five experimental runs.

The upper spectra in Fig. 7(a) display the 3156 cm^{-1} line after annealing at 260 K with the stress released, allowing the defect to relax back to thermal equilibrium. The polarization ratio of the mode, $R = I_\parallel/I_\perp$, returns to 1, its initial value before the stress-induced alignment. Fig. 7(b) presents the values of R observed in a similar experiment on the same sample through a series of relaxation anneals (20 min) at progressively higher temperatures (see also Fig. 5(a)). After each anneal, the sample was cooled to low temperature for the measurement of the polarized IR spectra. Notably, the O–H groups realign in a temperature range of about 160 to 200 K,

consistent with the temperature range required to induce their reorientation under stress.

In the context of the H$_i$ model, the observed alignment and relaxation of the 3156 cm^{-1} mode result from the thermalization of the two stress-induced nonequivalent O–H subgroups A and B. The [100] stress applied to the sample causes these defect configurations to exhibit different ground-state energies, which are populated according to Boltzmann statistics. The reoccupation of the O–H groups during the annealing treatments occurs through elementary hydrogen jumps between the A and B subgroups. Our calculations reveal that the easiest transition of this kind is the "hop" with an energy barrier of 0.59 eV to neighboring H sites located in the same c channel. Jumps to adjacent c channels are notably less favorable. We also note that the in-ab-plane motion across the c channel (see transition O$_1 \rightarrow$ O$_2$ in Figs. 2, 3, and 5(c)), featuring an estimated energy barrier of only 0.22 eV, represents a jump between equivalent O–H units and is therefore inaccessible in our experiment.

The transition rate between two hydrogen sites depends on temperature as $r = \nu e^{-E_a/kT}$, where E_a is the activation energy, and ν is the "attempt rate". Using this equation and the experimental data from Fig. 7(b), we determined a best-fit value of $E_a = 0.57 \pm 0.04$ eV. Here, we assumed ν to be in the order of 10^{11}–10^{13} s^{-1}. Such frequencies are typical for hydrogen-related defects in oxides and characterize the local hydrogen vibrations [47,49–51]. Note that the attempt frequency has very little influence on the best-fit parameter for E_a [47]. Within experimental accuracy, the activation energy determined matches the migration barrier obtained through our theoretical calculations.

The results of our uniaxial-stress experiments corroborate the theoretical predictions regarding the microstructural and diffusion properties of the H$_i$ center in SnO$_2$. Given the substantial body of evidence supporting the assignment of H$_i$ to the 3156 cm^{-1} line, we will use both terms interchangeably throughout the text.

Interestingly, our findings for H$_i$ (or the 3156 cm^{-1} line) in SnO$_2$ bear a striking resemblance to those observed for its counterpart in rutile TiO$_2$, where H$_i$ exhibits an O–H stretch vibrational mode at around 3290 cm^{-1} and also locates in the open c channels of the crystal. The diffusion of hydrogen in rutile TiO$_2$ is highly anisotropic, with a significantly lower activation barrier in the c direction [49,52]. Uniaxial stress along [100] results in the splitting of the 3290 cm^{-1} line into two components, displaying stress patterns very similar to what we observed in our experiments on SnO$_2$ [49]. The defect alignment of H$_i$ in rutile TiO$_2$ under stress is observed at annealing temperatures exceeding 165 K, corresponding to an activation energy of 0.53 eV for hydrogen jumps to nearest-neighbor positions. In our assessment, these conspicuous similarities in the behavior of interstitial hydrogen in rutile SnO$_2$ and TiO$_2$ provide further support for the H$_i$ defect model of the 3156 cm^{-1} center.

B. Free carrier absorption and thermal stability

Figures 8(a) and 8(b) show unpolarized IR absorbance spectra recorded at 18 K for a (001)-plane cut CVT-grown SnO$_2$ sample. The wave vector $\boldsymbol{k}$ of the incident IR beam
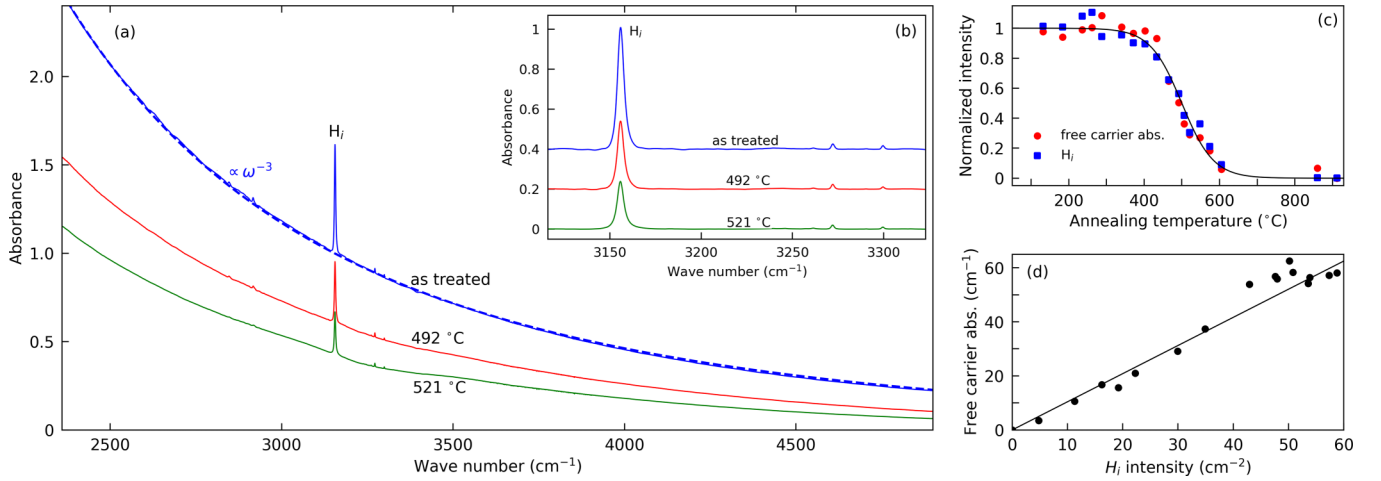
FIG. 8. (a) Sections of free-carrier absorption spectra (18 K) obtained on a hydrogenated CVT-grown sample with subsequent annealing treatments. The blue dashed line presents a fit of the absorption baseline to the power-law dependence $\omega^{-3} = \lambda^3$. (b) Baseline-corrected region of O–H stretch modes of the same spectra from section (a). (c) Normalized intensity of the H_i signal and free carrier absorption vs. annealing temperature. (d) Intensity correlation between H_i signal and free carrier absorption.

was aligned parallel to the [001] crystallographic axis. In section (a), we present an overview of the mid-infrared spectral range, while section (b) offers a closer look at the baseline-corrected region containing the O–H stretch modes. The uppermost spectra correspond to the sample hydrogenated at 600 °C, while the other ones represent spectra obtained during a series of annealing steps, each at a different temperature, as indicated in the figure.

The spectra reveal two prominent features: the sharp H_i mode at 3156 cm^{-1} and a broad low-frequency absorption. These features are absent in the nonhydrogenated CVT sample. The 3156 cm^{-1} IR peak dominates the O–H stretch mode spectral region, with only minor peaks at around 3272 and 3300 cm^{-1}, originating from single-hydrogen centers of unknown microscopic nature [17,21,22]. The spectra demonstrate that our CVT-grown samples exhibit low levels of residual impurities.

The intensity of the 3156 cm^{-1} H_i mode is strongest after hydrogenation and decreases during the annealing series. Concurrently, the broad featureless IR absorption also diminishes. The intensity of this absorption scales with frequency as ω^{-3}, indicative of free carrier absorption [53]. Indeed the introduction of free carriers by the hydrogenation of SnO$_2$ was also observed in previous studies [17,21,22]. Using the work of Summit and Borrelli [53], we estimate the electron concentration n in the as-treated sample to be $\sim 4 \times 10^{17}$ cm^{-3}.

In IR absorption, the concentration of absorbing species can be obtained from the intensity of the vibrational mode and the corresponding effective charge e^* [54]. In the reasonable assumption that all free carriers are due to H_i ($n = N_{3156}$) we may calibrate the 3156-cm^{-1} mode. If α denotes the absorption coefficient of the local mode, the effective charge can be estimated from [55]

$$A \equiv \int \alpha(\sigma) d\sigma = \frac{\pi e^{*2} N_{3156}}{nc^2 \mu_{O-H}}, \qquad (1)$$

where n is the refractive index, c is the velocity of light, μ_{O-H} is the reduced mass of the O–H bonds, and $\sigma = \lambda^{-1}$ is the wave number.

A value of 47 cm^{-2} was determined for the as-treated sample in Fig. 8. From here we obtain $e^* = (0.58 \pm 0.1)e$ with an error due to uncertainty in N_{3156} and sample orientation. We note that it is close to the one obtained earlier for interstitial hydrogen donor in ZnO, $e^* = 0.28e$ [56]. For practical purposes, Eq. (1) can be rewritten to allow a direct determination of the H_i concentration

$$N_{3156} = (1.0 \pm 0.2) \times 10^{16} \text{ cm}^{-1} \text{ A}. \qquad (2)$$

Figure 8(c) presents the normalized intensity of both the free carrier absorption (measured at 2500 cm^{-1}) and the H_i peak across the annealing series. Both features remain stable up to approximately 450 °C and disappear concurrently at higher annealing temperatures. Figure 8(d) demonstrates the linear intensity correlation between both signals, providing evidence for a common origin. We conclude that the H_i donor species dominates the electrical behavior of our hydrogenated CVT samples.

This behavior stands in contrast to earlier findings [17,21], where several hydrogen centers in SnO$_2$ were observed to interact and undergo interconversion during thermal treatments. We attribute these disparities in the experimental results to the high purity of our crystals and the "O-rich" hydrogenation method we employed. In the previous studies, the samples contained elevated levels of residual impurities or native defects, which readily trapped hydrogen due to its high mobility. Notably, in these studies, H_i was found to be unstable on a timescale of weeks at room temperature, whereas in our "trap-free" samples, H_i remained stable.

To summarize this subsection, the CVT-grown samples employed in our study exhibit high purity and structural quality. The linear intensity correlation observed between H_i and the free carrier absorption provides direct evidence of the shallow donor behavior of H_i centers.
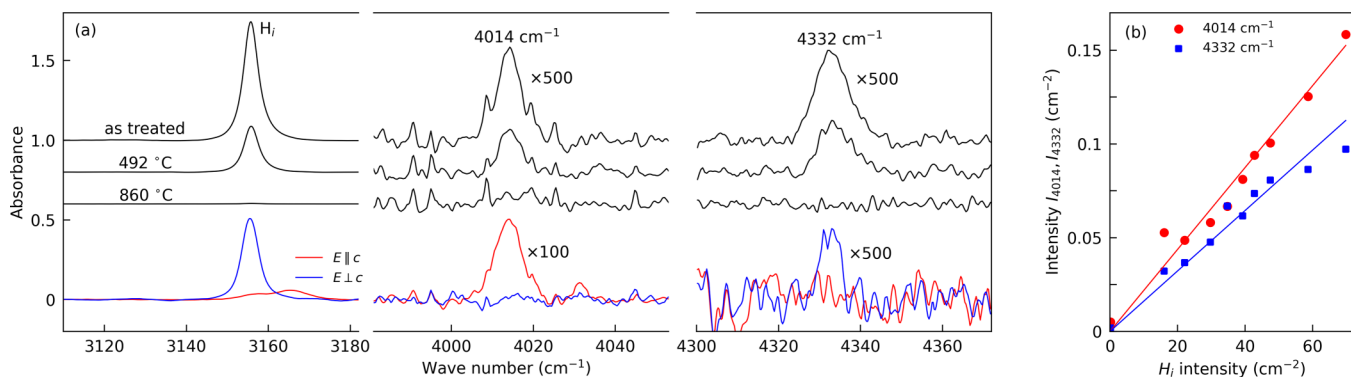
FIG. 9. (a) Sections of IR absorbance spectra recorded at 40 K for two different SnO_2 samples. The upper spectra represent unpolarized data obtained from a hydrogenated CVT-grown sample during a series of annealing steps. The c-axis of this sample is nearly parallel to the wavevector $\mathbf{k}$ of the IR beam. The lower spectra show polarized data from a (100)-plane cut hydrogenated PVT-grown sample. (b) Intensity correlation between the H_i stretch mode and transitions with peak frequencies at $\sim$4014 and $\sim$4332 cm^{-1}. The data were obtained from the annealing series of the hydrogenated CVT sample.

C. Wag and combination modes

Figure 9(a) displays expanded IR absorbance spectra obtained for two different SnO_2 samples. The upper spectra were recorded on a CVT-grown sample subjected to hydrogenation and subsequent annealing steps. The crystallographic c axis of this sample was aligned nearly, but not fully parallel to the wave vector of the IR beam, allowing also transitions with dipole moments oriented parallel to c to be observed in the spectra.

In the spectra, the 3156 cm^{-1} stretch mode of H_i predominates (two very minor peaks at 3272 and 3300 cm^{-1} similar to that from Fig. 8(b) are not shown here). In addition, two previously unreported significantly weaker features at peak frequencies of $\sim$4014 and $\sim$4332 cm^{-1} are seen. Fig. 9(b) demonstrates the intensity correlation between these signals and the H_i stretch mode, as determined during the series of annealing treatments. The intensities of the 4014 and 4332 cm^{-1} transitions exhibit a linear relationship with the H_i stretch mode, suggesting a common origin for all these signals.

The peak frequencies of the two weaker features are consistent with stretch + wag combination modes commonly found in other oxides [57–59]. The frequency differences between these modes and the H_i stretch mode, i.e., $(4014 - 3156)$ cm^{-1} = 858 cm^{-1} and $(4332 - 3156)$ cm^{-1} = 1176 cm^{-1}, closely match the calculated out-of-ab-plane (862 cm^{-1}) and in-ab-plane wag mode frequencies (1158 cm^{-1}) of H_i (see Sec. III). It is worth noting that local mode analysis by theory is prone to relatively large systematic errors in vibrational frequencies, and combination mode frequencies are shifted from harmonic frequencies by anharmonicity effects [60].

Additional support for this assignment comes from polarized absorption data presented in the lower section of Fig. 9(a). These spectra were recorded on a hydrogenated (100)-plane cut PVT-grown sample. The transition moment of the 4332 cm^{-1} line is aligned in the ab plane of the crystal, as expected for the combination of the H_i stretch and in-plane wag modes. In contrast, the 4014 cm^{-1} signal exhibits predominant polarization parallel to the c axis due to contributions from the out-of-ab-plane wag mode.

Attempts to directly observe the two fundamental wag modes of H_i by IR absorption spectroscopy were hindered by the spectral region of about 800–1200 cm^{-1}, where both modes are expected, being inaccessible due to strong free carrier and/or two-phonon lattice absorption.

In conclusion, the consistency observed in our data on combinational modes provides further evidence supporting the H_i defect model for the 3156 cm^{-1} line.

D. Excitonic absorption and photoluminescence

The complexity of near-band-edge transitions in SnO_2 has been well-documented for over 50 years [29,61–64]. The band structure of SnO_2 exhibits high anisotropy, leading to distinct optical behaviors depending on the orientation of incident light. For light polarized parallel to the crystallographic c axis, the absorption edge initiates at photon energies of approximately 3.5 eV and shifts to higher energies as the temperature decreases. It maintains a broad and featureless profile, largely unaffected by temperature variations. Conversely, for light polarized perpendicular to the c axis, the fundamental absorption edge appears about 0.4 eV lower in energy. It manifests a hydrogenlike series of sharp excitonic lines at low temperature. These excitonic features, initially observed by Nagasawa *et al.* [61–63], are overspread above 100 K by an exponential Urbach tail, attributed to transitions originating from deeper valence bands.

The band symmetry of SnO_2 is such that excitonic transitions across the band gap at precisely $\mathbf{k} = 0$ are dipole-forbidden [62,63]. However, they become allowed when considering the $\mathbf{k}$-space away from the direct band gap region. Consequently, a typical band-edge spectrum includes a weak, quadrupole-allowed 1s free exciton (FE) line at approximately 3.564 eV at 4 K, accompanied by a series of 2p, 3p, and higher-order excitonic transitions on the higher energy side.

In certain SnO_2 crystals, transitions appearing at lower energies adjacent to the 1s free exciton peak have been observed [28,29,63,65]. These transitions have been interpreted as signals from bound excitons (BE) localized at
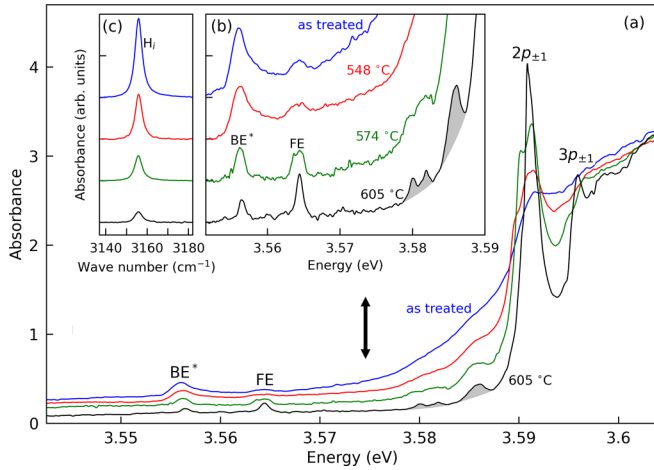
FIG. 10. (a) Sections of near band edge absorption spectra recorded on *c*-plane cut CVT grown SnO$_2$ sample taken at 9 K. The sample was first hydrogenated at 600 °C and then subsequently annealed at the temperatures shown. (b) Zoomed-in region of the same spectra. (c) Baseline-corrected IR absorption spectra measured for the same sample as for section (a) and (b).
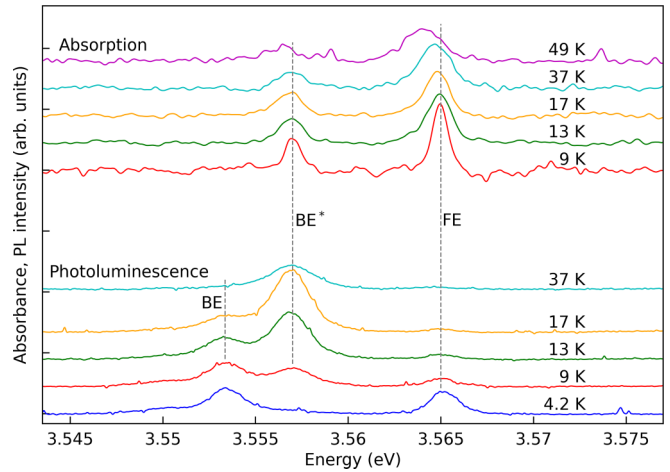

FIG. 11. Temperature-dependent absorbance and photoluminescence spectra as obtained on a hydrogenated CVT grown sample subjected to a subsequent annealing at 605 °C.

shallow donor centers associated with intrinsic defects or impurities [29,65]. Unlike the 1*s* FE transition, these lines possess dipole character, enabling their observation even at relatively low defect concentrations, down to the order of 10^{16} cm^{-3}.

The presence of excitonic features in absorption or photoluminescence spectra heavily depends on the purity and structural quality of the SnO$_2$ crystals. Unintentional impurities or electric fields induced by random crystal imperfections significantly contribute to broadening the electronic states. From a spectroscopic perspective, crystals grown via CVT method have consistently demonstrated superior results [29,61–63,65]. In this study, we utilize our high-quality CVT samples to investigate the excitonic behavior associated with the H$_i$ shallow donor defect.

Figure 10(a) displays UV absorbance spectra recorded at 9 K on a hydrogenated *c*-plane cut CVT sample. The uppermost spectrum (blue) corresponds to the as-treated sample hydrogenated at 600 °C, while the subsequent spectra represent data obtained during a series of sequential annealing steps at varying temperatures. Section (b) of the figure provides a close-up view of the same spectra. Section (c) presents the IR absorbance of the H$_i$ stretch mode recorded on the same sample along with UV absorbance measurements after each annealing step. Notably, the H$_i$ signal is most pronounced immediately after hydrogenation and gradually diminishes during the annealing series, consistent with our previous observations.

The spectra reveal a substructure in the near-band-edge region that is broadened for the as-treated sample and progressively sharpens during the annealing series. Simultaneously, the Urbach tail at about 3.58–3.59 eV experiences a significant reduction, an effect which we attributed to the decreasing H$_i$ concentration.

Based on their spectral positions, we identify the signal at ∼3.564 eV as the 1*s* free exciton line (FE), whereas the

peaks at ∼3.59 and 3.595 eV originate from the 2*p* and 3*p* FE transitions, respectively. The position of the signal labeled BE* matches those previously attributed to bound excitons of shallow donor centers [29]. Importantly, the intensity of BE* correlates with that of the H$_i$ stretch mode. Furthermore, we identify a substructure of signals between 3.58 and 3.587 eV, shown shaded in gray in Fig. 10(b). Similar features have been observed in Sb-doped SnO$_2$ single crystals and interpreted as higher-order states of the exciton complexes bound to the shallow Sb donor [29]. The observation of H$_i$-related excitonic fine structure is an important finding and provides evidence of the shallow-donor-like behavior of this defect.

Figure 11 presents temperature-dependent absorbance and photoluminescence spectra recorded on the 605 °C annealed sample from Figure 10. It can be seen that the BE* and FE absorption signals broaden as the temperature increases. At 49 K, a clear shift of the peak positions toward lower energies is observed, attributed to a reduction in the fundamental band gap. It is noteworthy that within experimental accuracy, the integrated peak intensities of both transitions, as well as their relative intensities, remain constant up to the highest measured temperature (60 K).

The BE* and FE lines also appear in our photoluminescence spectra. Interestingly, a new signal at approximately 3.5535 eV, labeled as BE, emerges. Photoluminescence lines at this position were previously observed in reduced SnO$_2$ crystals [28,65]. It was suggested that the BE* and BE transitions share a common microscopic defect origin, though specific details on the nature of these recombination lines remain unclear. Our complete set of experimental data supports this conclusion. We find that, under given experimental parameters such as temperature and laser power, the relative intensities of both signals are independent of the sample's history, while absolute intensities may exhibit significant variability. Considering that H$_i$ is the predominant shallow donor defect in our hydrogenated samples, we propose that the BE* and BE transitions in our spectra correspond to different exciton transitions bound to the same H$_i$ donor.
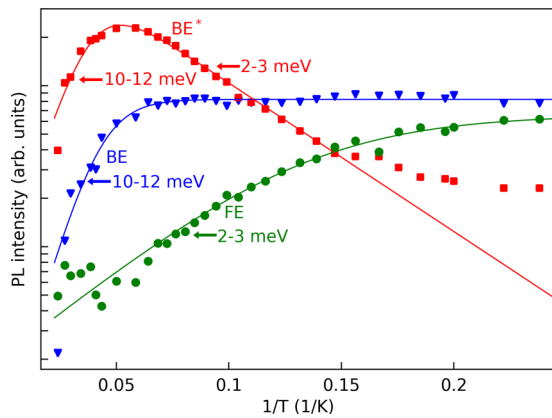
FIG. 12. Arrhenius plot of the FE, BE*, and BE PL intensites as obtained on a hydrogenated CVT grown sample subjected to a subsequent annealing at 605 °C. Solid lines are best-fit curves of thermal quenching behavior to the data (see text for details). The respective activation energies obtained from the fitting procedure are given.

Figure 12 presents an Arrhenius plot of photoluminescence intensities obtained from the 605 °C annealed sample. As the temperature increases, the photoluminescence signal associated with the free exciton gradually decreases. The data presented in Fig. 11 demonstrate that in absorption measurements the $1s$ free exciton line remains relatively constant up to significantly higher temperatures. Therefore the quenching of the FE photoluminescence line with increasing temperature cannot be attributed to a thermal decay of the free excitons but rather results from an increase in competitive nonradiative recombination channels. To analyze the dissociation of this transition, we employed an Arrhenius-type single rate relation $I(T)/I(0\ \mathrm{K}) = 1/(1 + A\exp(-E_a/kT))$, where A and E_a represent the prefactor and activation energy of a thermally activated nonradiative recombination process (see, e.g., Refs. [66,67]). As shown in Fig. 12, this equation adequately describes the thermal behavior of FE and provides an activation energy estimate of 2–3 meV.

In contrast, the BE line remains nearly constant until approximately 14 K, beyond which it rapidly diminishes. The activation energy associated with the decay of the BE recombination lines falls within the range of 10 to 12 meV. This value matches the so-called localization energy of the transition, defined as the energy separation between its peak position and that of the FE signal (here 11.5 meV). In the context of excitonic behavior, this indicates that the BE complex dissociates by releasing a free exciton.

The BE* line exhibits a thermally activated behavior, initially increasing in intensity and then decreasing at high temperatures. To account for the increase in BE* at low temperatures, we have additionally included a thermally activated process expressed by the activation energy E_b: $I(T)/I(0\ \mathrm{K}) = \exp(-E_b/kT)/(1 + A\exp(-E_a/kT))$. The corresponding activation energies, obtained from the fitting procedure, are provided in Fig. 12. The thermal quenching of BE* at high temperatures occurs with an activation energy of 10 to 12 meV, similar to that observed for the BE line, suggesting a correlated dissociation process of these states to free exciton.

The observed increase in BE* intensity at low temperatures indicates the involvement of excited states associated with the bound exciton. Several scenarios have been proposed in the literature to explain similar behavior observed in the photoluminescence spectra of other semiconductors [67–69]. These scenarios include excitons that involve a hole from the B- instead of the A-valence band, vibrational-rotational excited states of the excitons, or electronic excited states of the excitons.

The choice between these models cannot be definitively made solely from the present investigation. A noteworthy feature of the BE* activation is its activation energy of 2–3 meV, being close to that observed for the quenching of the FE signal as well as the spectral separation between the BE and BE* positions (3.5 meV). An involvement of a higher-lying conduction or deper-lying valence band in the BE* transition could, in principle, explain such a behavior. The detailed band structure of SnO₂, however, is very complicated, with limited information on the conduction and valence band ordering available so far. Excitonic series of holes from split-off B- and C-valence bands have been observed by two-photon spectroscopy [70], however, their energetic distance from the A exciton series of about 50 and 105 meV, respectively, is much higher than the thermal activation energy of the BE* transition. We conclude that a comprehensive study of the exciton kinetics, including also magnetooptical and photoluminescence excitation spectroscopy, is necessary to elucidate the nature of the BE* recombination line.

V. CONCLUSIONS

The nature of interstitial hydrogen in SnO₂ has been elucidated through a comprehensive investigation, encompassing first-principles theory, and various spectroscopic techniques, including infrared absorption, near band-edge absorption, and photoluminescence spectroscopy. This collective approach reaffirms the earlier interpretation of a center exhibiting an O–H stretch mode at $3156\ \mathrm{cm}^{-1}$ as interstitial hydrogen. Our uniaxial stress experiments targeting the $3156\ \mathrm{cm}^{-1}$ mode unveil the precise location of the interstitial hydrogen atom within the open c channel of the rutile SnO₂ structure. Migration along the c axis of the crystals occurs via low barrier hydrogen jumps of around 0.57 eV to symmetrically equivalent nearest-neighbor positions. Combinational vibrations of this O–H stretch mode with the out-of-ab-plane and in-ab-plane wag modes at about 4014 and $4332\ \mathrm{cm}^{-1}$ have been identified. In high-purity, "trap-free" crystals, H_i remains thermally stable up to an annealing temperature of around 450 °C. Through investigations into free carrier absorption and excitonic properties, we have unveiled that H_i forms an effective shallow-donor-like state, akin to the well-characterized F, Cl, and Sb n-type dopants in this material. Our results underscore the significance of interstitial hydrogen for carrier statistics and applications of SnO₂.

[1] R. E. Presley, C. L. Munsee, C.-H. Park, D. Hong, J. F. Wager, and D. A. Keszler, Tin oxide transparent thin-film transistors, J. Phys. D: Appl. Phys. **37**, 2810 (2004).

[2] N. Kikuchi, E. Kusano, E. Kishio, and A. Kinbara, Electrical and mechanical properties of SnO_2:Nb films for touch screens, Vacuum **66**, 365 (2002).

[3] N. S. Murty and S. R. Jawalekar, Characterization of antimony-doped tin oxide films for solar cell applications, Thin Solid Films **108**, 277 (1983).

[4] M. Batzill and U. Diebold, The surface and materials science of tin oxide, Prog. Surf. Sci. **79**, 47 (2005).

[5] A. Tischner, T. Maier, C. Stepper, and A. Köck, Ultrathin SnO_2 gas sensors fabricated by spray pyrolysis for the detection of humidity and carbon monoxide, Sens. Actuators B: Chem. **134**, 796 (2008).

[6] S. B. Ogale, R. J. Choudhary, J. P. Buban, S. E. Lofland, S. R. Shinde, S. N. Kale, V. N. Kulkarni, J. Higgins, C. Lanci, J. R. Simpson, N. D. Browning, S. Das Sarma, H. D. Drew, R. L. Greene, and T. Venkatesan, High temperature ferromagnetism with a giant magnetic moment in transparent Co-doped $SnO_{2-\delta}$, Phys. Rev. Lett. **91**, 077205 (2003).

[7] Z. M. Jarzebski, Physical properties of SnO_2 materials: II. Electrical properties, J. Electrochem. Soc. **123**, 299C (1976).

[8] C. G. Fonstad and R. H. Rediker, Electrical properties of high-quality stannic oxide crystals, J. Appl. Phys. **42**, 2911 (1971).

[9] S. Samson and C. G. Fonstad, Defect structure and electronic donor levels in stannic oxide crystals, J. Appl. Phys. **44**, 4618 (1973).

[10] M. Nagasawa and S. Shionoya, Properties of oxidized SnO_2 single crystals, Jpn. J. Appl. Phys. **10**, 727 (1971).

[11] Ç. Kılıç and A. Zunger, *n*-type doping of oxides by hydrogen, Appl. Phys. Lett. **81**, 73 (2002).

[12] A. K. Singh, A. Janotti, M. Scheffler, and C. G. Van de Walle, Sources of electrical conductivity in SnO_2, Phys. Rev. Lett. **101**, 055502 (2008).

[13] D. O. Scanlon and G. W. Watson, On the possibility of *p*-type SnO_2, J. Mater. Chem. **22**, 25236 (2012).

[14] J. Robertson and P. W. Peacock, Doping and hydrogen in wide gap oxides, Thin Solid Films **445**, 155 (2003).

[15] K. Xiong, J. Robertson, and S. J. Clark, Behavior of hydrogen in wide band gap oxides, J. Appl. Phys. **102**, 083710 (2007).

[16] J. B. Varley, A. Janotti, A. K. Singh, and C. G. Van de Walle, Hydrogen interactions with acceptor impurities in SnO_2: First-principles calculations, Phys. Rev. B **79**, 245206 (2009).

[17] W. M. Hlaing Oo, S. Tabatabaei, M. D. McCluskey, J. B. Varley, A. Janotti, and C. G. Van de Walle, Hydrogen donors in SnO_2 studied by infrared spectroscopy and first-principles calculations, Phys. Rev. B **82**, 193201 (2010).

[18] H. F. Kunkle and E. E. Kohnke, Flux growth of stannic oxide crystals, J. Appl. Phys. **36**, 1489 (1965).

[19] P. Turkes, C. Pluntke, and R. Helbig, Thermal conductivity of SnO_2 single crystals, J. Phys. C: Solid State Phys. **13**, 4941 (1980).

[20] P. D. C. King, R. L. Lichti, Y. G. Celebi, J. M. Gil, R. C. Vilão, H. V. Alberto, J. Piroto Duarte, D. J. Payne, R. G. Egdell, I. McKenzie, C. F. McConville, S. F. J. Cox, and T. D. Veal, Shallow donor state of hydrogen in In_2O_3 and SnO_2: Implications for conductivity in transparent conducting oxides, Phys. Rev. B **80**, 081201(R) (2009).

[21] F. Bekisli, M. Stavola, W. B. Fowler, L. Boatner, E. Spahr, and G. Lüpke, Hydrogen impurities and shallow donors in SnO_2 studied by infrared spectroscopy, Phys. Rev. B **84**, 035213 (2011).

[22] F. Herklotz, I. Chaplygin, E. V. Lavrov, and V. F. Agekyan, Photoconductive detection of a hydrogen-related donor in SnO_2, Appl. Phys. Lett. **114**, 152103 (2019).

[23] K. Watanabe, I. Sakaguchi, M. Hashiguchi, N. Saito, E. M. Ross, H. Haneda, T. Ohsawa, and N. Ohashi, Isotope tracer investigation and *ab-initio* simulation of anisotropic hydrogen transport and possible multi-hydrogen centers in tin dioxide, J. Appl. Phys. **119**, 225704 (2016).

[24] R. S. Katiyar, P. Dawson, M. M. Hargreave, and G. R. Wilkinson, Dynamics of the rutile structure. III. Lattice dynamics, infrared and Raman spectra of SnO_2, J. Phys. C: Solid State Phys. **4**, 2421 (1971).

[25] J. Maldener, F. Rauch, M. Gavranic, and A. Beran, OH absorption coefficients of rutile and cassiterite deduced from nuclear reaction analysis and FTIR spectroscopy, Mineral Petrol. **71**, 21 (2001).

[26] Z. Losos and A. Beran, OH defects in cassiterite, Mineral Petrol. **81**, 219 (2004).

[27] M. Stavola, F. Bekisli, W. Yin, K. Smithe, B. W. Fowler, and L. A. Boatner, Contrasting the experimental properties of hydrogen in SnO_2, In_2O_3, and TiO_2, J. Appl. Phys. **115**, 012001 (2014).

[28] V. F. Aguekian, Y. A. Stepanov, I. Akai, T. Karasawa, and T. Komatsu, Exciton luminescence in tin dioxide single crystals, J. Phys. Soc. Jpn. **62**, 4516 (1993).

[29] V. T. Agekyan, Spectroscopic properties of semiconductor crystals with direct forbidden energy gap, Phys. Status Solidi A **43**, 11 (1977).

[30] Z. Galazka, R. Uecker, D. Klimm, K. Irmscher, M. Pietsch, R. Schewski, M. Albrecht, A. Kwasniewski, S. Ganschow, D. Schulz, C. Guguschev, R. Bertram, M. Bickermann, and R. Fornari, Growth, characterization, and properties of bulk SnO_2 single crystals, Phys. Status Solidi A **211**, 66 (2014).

[31] Z. Galazka, *Transparent Semiconducting Oxides: Bulk Crystal Growth and Fundamental Properties* (Jenny Stanford Publishing, 2020).

[32] Z. Galazka, K. Irmscher, M. Pietsch, S. Ganschow, D. Schulz, D. Klimm, I. M. Hanke, T. Schroeder, and M. Bickermann, Experimental Hall electron mobility of bulk single crystals of transparent semiconducting oxides, J. Mater. Res. **36**, 4746 (2021).

[33] P. E. Blöchl, Projector augmented-wave method, Phys. Rev. B **50**, 17953 (1994).

[34] J. P. Perdew, A. Ruzsinszky, G. I. Csonka, O. A. Vydrov, G. E. Scuseria, L. A. Constantin, X. Zhou, and K. Burke, Restoring the density-gradient expansion for exchange in solids and surfaces, Phys. Rev. Lett. **100**, 136406 (2008).

[35] P. Giannozzi, S. Baroni, N. Bonini, M. Calandra, R. Car, C. Cavazzoni, D. Ceresoli, G. L. Chiarotti, M. Cococcioni, I. Dabo, A. D. Corso, S. de Gironcoli, S. Fabris, G. Fratesi, R. Gebauer, U. Gerstmann, C. Gougoussis, A. Kokalj, M. Lazzeri, L. Martin-Samos *et al.*, QUANTUM ESPRESSO: a modular and open-source software project for quantum simulations of materials, J. Phys.: Condens. Matter **21**, 395502 (2009).

[36] P. Giannozzi Jr., O. Andreussi, T. Brumme, O. Bunau, M. B. Nardelli, M. Calandra, R. Car, C. Cavazzoni, D. Ceresoli, M. Cococcioni, N. Colonna, I. Carnimeo, A. D. Corso, S. de Gironcoli, P. Delugas, R. A. DiStasio, A. Ferretti, A. Floris, G. Fratesi, G. Fugallo *et al.*, Advanced capabilities for materials modelling with quantum ESPRESSO, J. Phys.: Condens. Matter **29**, 465901 (2017).

[37] We used the pseudopotentials Sn.pbesol-dn-kjpaw_psl.1.0.0.UPF, O.pbesol-n-kjpaw_psl.1.0.0.UPF, and H.pbesol-kjpaw_psl.1.0.0.UPF from the Quantum ESPRESSO PSlibrary.

[38] SnO$_2$ rutile-type (SnO$_2$) crystal structure: Datasheet from "pauling file multinaries edition – 2022", copyright 2023 Springer-Verlag Berlin Heidelberg & Material Phases Data System (MPDS), Switzerland & National Institute for Materials Science (NIMS), Japan, Part of SpringerMaterials.

[39] S. Baroni, S. de Gironcoli, A. Dal Corso, and P. Giannozzi, Phonons and related crystal properties from density-functional perturbation theory, Rev. Mod. Phys. **73**, 515 (2001).

[40] J. B. Varley, H. Peelaers, A. Janotti, and C. G. Van de Walle, Hydrogenated cation vacancies in semiconducting oxides, J. Phys.: Condens. Matter **23**, 334212 (2011).

[41] M. Stavola, S. J. Pearton, J. Lopata, C. R. Abernathy, and K. Bergman, Structure and dynamics of the Be–H complex in GaAs, Phys. Rev. B **39**, 8051 (1989).

[42] D. M. Kozuch, M. Stavola, S. J. Spector, S. J. Pearton, and J. Lopata, Symmetry, stress alignment, and reorientation kinetics of the Si$_{As}$–H complex in GaAs, Phys. Rev. B **48**, 8751 (1993).

[43] G. D. Watkins and J. W. Corbett, Defects in irradiated silicon. I. Electron spin resonance of the Si-*A* center, Phys. Rev. **121**, 1001 (1961).

[44] M. Stavola, K. Bergman, S. J. Pearton, and J. Lopata, Hydrogen motion in defect complexes: Reorientation kinetics of the B-H complex in silicon, Phys. Rev. Lett. **61**, 2786 (1988).

[45] Y. M. Cheng and M. Stavola, Non-arrhenius reorientation kinetics for the B–H complex in Si: Evidence for thermally assisted tunneling, Phys. Rev. Lett. **73**, 3419 (1994).

[46] M. Stavola, Y. M. Cheng, and G. Davies, Al–H and Al–D complexes in Si: A uniaxial-stress study of the hydrogen vibrational modes, Phys. Rev. B **54**, 11322 (1996).

[47] F. Börrnert, E. V. Lavrov, and J. Weber, Hydrogen motion in the Cu-H complex in ZnO, Phys. Rev. B **75**, 205202 (2007).

[48] E. V. Lavrov, J. Weber, and F. Börrnert, Copper dihydrogen complex in ZnO, Phys. Rev. B **77**, 155209 (2008).

[49] A. J. Hupfer, E. V. Monakhov, B. G. Svensson, I. Chaplygin, and E. V. Lavrov, Hydrogen motion in rutile TiO$_2$, Sci. Rep. **7**, 17065 (2017).

[50] I. Chaplygin, F. Herklotz, and E. V. Lavrov, Reorientation kinetics of hydroxyl groups in anatase TiO$_2$, J. Chem. Phys. **149**, 044507 (2018).

[51] P. Weiser, Y. Qin, W. Yin, M. Stavola, W. B. Fowler, and L. A. Boatner, Symmetry and diffusivity of the interstitial hydrogen shallow-donor center in In$_2$O$_3$, Appl. Phys. Lett. **109**, 202105 (2016).

[52] O. W. Johnson, S.-H. Paek, and J. W. DeFord, Diffusion of H and D in TiO$_2$: Suppression of internal fields by isotope exchange, J. Appl. Phys. **46**, 1026 (1975).

[53] R. Summitt and N. Borrelli, Infrared absorption in single crystal stannic oxide, J. Phys. Chem. Solids **26**, 921 (1965).

[54] R. C. Newman, *Imperfections in III/V Materials*, edited by E. R. Weber, Semiconductors and Semimetals (Academic Boston, San Diego, 1993), Vol. 38.

[55] E. B. Wilson, J. C. Decius, and P. C. Cross, *Molecular Vibrations* (Dover, New York, 1980).

[56] E. V. Lavrov, F. Herklotz, and J. Weber, Identification of two hydrogen donors in ZnO, Phys. Rev. B **79**, 165210 (2009).

[57] A. Grone and S. Kapphan, Combination bands of libration+vibration of OH/OD centres in ABO$_3$ crystals, J. Phys.: Condens. Matter **7**, 3051 (1995).

[58] E. J. Spahr, L. Wen, M. Stavola, L. A. Boatner, L. C. Feldman, N. H. Tolk, and G. Lüpke, Proton tunneling: A decay channel of the O–H stretch mode in KTaO$_3$, Phys. Rev. Lett. **102**, 075506 (2009).

[59] E. J. Spahr, L. Wen, M. Stavola, L. A. Boatner, L. C. Feldman, N. H. Tolk, and G. Lüpke, Giant enhancement of hydrogen transport in rutile TiO$_2$ at low temperatures, Phys. Rev. Lett. **104**, 205901 (2010).

[60] M. Stavola and W. B. Fowler, Tutorial: Novel properties of defects in semiconductors revealed by their vibrational spectra, J. Appl. Phys. **123**, 161561 (2018).

[61] M. Nagasawa and S. Shionoya, Exciton structure in optical absorption of SnO$_2$ crystals, Phys. Lett. **22**, 409 (1966).

[62] M. Nagasawa and S. Shionoya, Zeeman effect and symmetry of the intrinsic SnO$_2$ exciton, Phys. Rev. Lett. **21**, 1070 (1968).

[63] M. Nagasawa and S. Shionoya, Second class exciton structure in stannic oxide, J. Phys. Soc. Jpn. **30**, 158 (1971).

[64] V. T. Agekyan, Exciton absorption and symmetry of energy levels in SnO$_2$, Opt. Spectrosc. (USSR) **29**, 395 (1970).

[65] V. F. Agekian, A. Y. Serov, and N. G. Filosofov, Light emission from tin-dioxide crystals, Semiconductors **48**, 442 (2014).

[66] D. Bimberg, M. Sondergeld, and E. Grobe, Thermal dissociation of excitons bounds to neutral acceptors in high-purity GaAs, Phys. Rev. B **4**, 3451 (1971).

[67] M. Leroux, N. Grandjean, B. Beaumont, G. Nataf, F. Semond, J. Massies, and P. Gibart, Temperature quenching of photoluminescence intensities in undoped and doped GaN, J. Appl. Phys. **86**, 3721 (1999).

[68] B. K. Meyer, H. Alves, D. M. Hofmann, W. Kriegseis, D. Forster, F. Bertram, J. Christen, A. Hoffmann, M. Straßburg, M. Dworzak, and U. Haboeck, Bound exciton and donor-acceptor pair recombination in ZnO, Phys. Status Solidi B **241**, 231 (2004).

[69] B. K. Meyer, J. Sann, S. Eisermann, S. Lautenschlaeger, M. R. Wagner, M. Kaiser, G. Callsen, J. S. Reparaz, and A. Hoffmann, Excited state properties of donor bound excitons in ZnO, Phys. Rev. B **82**, 115207 (2010).

[70] K. Reimann and M. Steube, Experimental determination of the electronic band structure of SnO$_2$, Solid State Commun. **105**, 649 (1998).